IPEM
Institute of Physics and
Engineering in Medicine

PAPER

Optimized Monte Carlo simulations for voxel-based internal dosimetry

To cite this article: Leanderson P Cordeiro *et al* 2023 *Phys. Med. Biol.* **68** 115004
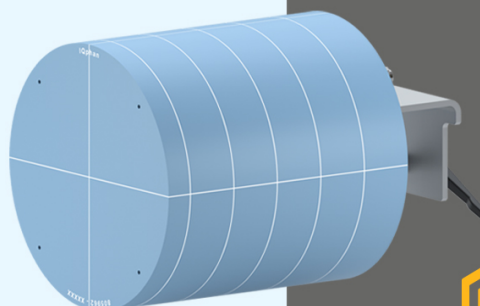
View the article online for updates and enhancements.

Physics in Medicine & Biology

IPEM
Institute of Physics and
Engineering in Medicine

PAPER

Optimized Monte Carlo simulations for voxel-based internal dosimetry

Leanderson P Cordeiro[1] , **Lidia V de Sá**[1], **Rafael A Kitamikado**[2] , **Marcelo T Sapienza**[2] and **Daniel A B Bonifacio**[1,3]

1 Institute of Radiation Protection and Dosimetry (IRD), Rio de Janeiro, Brazil
2 Hospital das Clínicas da Universidade de São Paulo (HCFMUSP), São Paulo, Brazil
3 Nuclear and Energy Research Institute (IPEN), São Paulo, Brazil

E-mail: leandersonpc88@gmail.com

Abstract

Objective. The scientific community has considered internal dosimetry by the Monte Carlo method the gold standard. However, there is a trade-off between simulation processing time and the statistical quality of the results that makes it a challenge to obtain accurate absorbed dose values in some situations, such as dose estimation in organs affected by cross-irradiation or limited computing power. Variance reduction techniques are used to reduce computational processing time without impairing the statistical quality of the results, such as tracking energy cutoff, secondary particle production threshold, and parallelism of different types of emissions from radionuclides. *Approach.* In this work, GATE Monte Carlo code and its variance reduction techniques were evaluated to calculate *S* values of organs from the international commission on radiological protection (ICRP) report 110 male phantom for the lutetium-177, iodine-131, yttrium-90, and radium-223 radionuclides. The results are compared with the data from the OpenDose collaboration. *Main results.* A cutoff of 5 MeV for local electron deposition and 2.0 mm of secondary particle production range resulted in a computational efficiency increase of 7.9 and 1.05 times, respectively. Simulation of ICRP 107 spectra-based source proved to be about 5 times more efficient when compared to a decay simulation using `G4RadioactiveDecay` (Geant4-based radioactive decay processes). Track length estimator (TLE) and split exponential track length estimator (seTLE) techniques were used to calculate the absorbed dose of photon emissions, resulting in computational efficiency up to 29.4 and 62.5 times higher when compared to traditional simulations, respectively. In particular, the seTLE technique accelerates the simulation time by up to 1426 times, achieving a statistical uncertainty of 10% in volumes affected by cross-irradiation. *Significance.* The variance reduction techniques used in this work drastically reduced the simulation time and maintained the statistical quality of the calculated absorbed dose values, proving the feasibility of the use of the Monte Carlo method in internal dosimetry under challenging situations and making it viable for clinical routine or web applications.

1. Introduction

Dosimetry in radionuclide therapy depends on estimating the amount of energy deposited in target organs or volumes of interest by particles emitted from regions with radiopharmaceutical uptake (Sgouros *et al* 2020).

A promising approach of personalized dosimetry for radionuclide therapy is based on Monte Carlo simulations using patient data, including molecular imaging such as positron emission tomography (PET) and single-photon emission computed tomography (SPECT), to define the regions of interest (e.g. tumors), and the anatomy modeling using computed tomography (CT) images. This approach allows for a more detailed voxel-based absorbed dose calculation than the organ-based method (Bolch *et al* 2009). However, Monte Carlo simulations are computationally intensive to solve problems with complex geometry requiring high statistical

precision, as is the case of absorbed dose calculations, which makes very challenging the implementation of this application in clinical routine or web-based software.

As a solution, the computational parallelism, through the use of logic devices such as graphics processing unit (GPU) and field programmable gate array (FPGA), has been proposed (Abhyankar *et al* 2019, Frezza *et al* 2020, Peng, *et al* 2020). However, some studies propose the use of the more cost-effective variance reduction techniques (VRTs) to speed up absorbed dose calculations. The Monte Carlo code GATE (Geant4 Application for Emission Tomography) (Jan *et al* 2004, 2011, Sarrut *et al* 2014, 2021) provides VRTs that can be used in absorbed dose calculations to reduce computational processing time, such as the energy cutoff used to limit Bremsstrahlung production and transport, capable of reducing simulation time and keeping global statistical uncertainties below 1% (EL Bakkali *et al* 2017). Previous works use distance thresholds for the production of secondary particles on PET modeling (Bonifacio *et al* 2010), improving simulation efficiency in estimates of specific absorbed fractions of photons (Lamrabet *et al* 2021), optimizing simulations for whole-body planar scintigraphic acquisitions (Costa *et al* 2017), and cell-based dosimetry (Pinto *et al* 2020). Previous works (Frezza *et al* 2020, Pareja García *et al* 2021) addressed this theme and showed motivating results.

In this work, several VRTs are combined and implemented in GATE for internal absorbed dose calculations and evaluated in terms of computational efficiency to optimize processing time while maintaining statistical quality, enabling its use in clinical routine and web-based software, such as the IRDose (Internal Radiation Dosimetry) web application (Bonifacio *et al* 2021).

2. Methods

To compare simulated results with and without the use of VRTs, *S* values of some organs from the adult male voxelized reference computational phantom of the international commission on radiological protection (ICRP) report 110 (Grosswendt 2012) were calculated. The radionuclides and source/target volumes were chosen according to the affinity criteria and/or organs at risk in their respective therapies. Source organs are those that uptake a certain amount of the administered radiopharmaceutical and their absorbed dose is determined by self-irradiation. Target organs are irradiated by radiation from the source organ(s). If we want to estimate the absorbed dose in an organ due to its self-irradiation, this organ is considered the source and target at the same time. This work considered four radionuclides typically used in nuclear medicine:

(a) lutetium-177: liver (target and source), kidneys (target), gall bladder wall (target), and gall bladder contents (source);

(b) iodine-131: salivary glands (target and source), lungs (target), stomach wall (target), and stomach contents (source);

(c) yttrium-90: liver (target and source), kidneys (target), lungs (target);

(d) radium-223: intestine wall (target), intestine contents (source) liver (target and source), kidneys (target).

The accumulated activity is used to compute the *S* values. At the simulation level, accumulated activity equals the number of events.

Simulations were run using GATE (Jan *et al* 2004) version 9.2 with `emstandard_opt4` physic list builder (Guide for physics lists 2022) and 10^7 events, and were performed on a PC based on the Intel Xeon E5-2670 v3 2.30 GHz (12 cores and 24 threads) and 32 GB RAM.

2.1. Voxelized anthropomorphic model
The ICRP 110 anthropomorphic model used in this work is composed of $254 \times 127 \times 222$ voxels for size of $2.137 \times 2.137 \times 8.0$ mm, corresponding to a height of 176 cm and a mass of 73 kg, with 141 segmented regions (figure 1).

2.2. MIRD formalism
The voxel-based dosimetry approach, applied in the ICRP 110 (Grosswendt 2012) voxelized phantom for absorbed dose calculation at segmented organs, allows us to apply the medical internal radiation dose (MIRD) formalism (Bolch *et al* 2009) for quantitative data of non-uniform activity distributions within target organs and/or volumes of interest (VOI), according to equation (1)

Figure 1. ICRP 110 voxelized virtual male phantom with the liver selected as source organ (viewed by 3D Slicer software (Fedorov *et al* 2012).

$$\overline{D}(\text{voxel}_k) = \sum_{h=0}^{N} \widetilde{A}_{\text{voxel}_h} \cdot S(\text{voxel}_k \leftarrow \text{voxel}_h), \tag{1}$$

where $\overline{D}(\text{voxel}_k)$ is the average absorbed dose in the target voxel (Gy), $\widetilde{A}_{\text{voxel}_h}$ is the number of nuclear decays in the source voxel (Bq$\cdots$) and $S(\text{voxel}_k \leftarrow \text{voxel}_h)$ is defined as the average absorbed dose in a target voxel by nuclear decay in the source voxel (Gy.Bq^{-1}.s^{-1}).

2.3. Dose map calculation

In the GATE environment, a tool called `DoseActor` stores the absorbed dose at voxel level in a 3D matrix (or dose map) in a raw image described by the open-source Insight Segmentation and Registration Toolkit (ITK) MetaImage Header (MHD), which is a text-based tagged file format for medical images. In addition to the absorbed dose represented by the voxel value, the dose map contains information about the image dimension,

voxel size, and data format. The `DoseActor` also stores the deposited energy, associated relative uncertainty, and the number of interactions, defined as hits by GATE/Geant4. The absorbed dose in a homogeneous region is determined by the average value of the absorbed doses in each voxel, according to equation (2):

$$\bar{d} = \frac{1}{N}\sum_{i=1}^{N} d_i.$$ (2)

The standard deviation of the mean $(\hat{d})$, in equation (5), is deduced by defining the unbiased variance estimator (σ^2) and the standard deviation (σ), defined in equations (3) and (4), respectively (Visvikis *et al* 2006).

$$\sigma^2 = \frac{1}{N^2}\left[N\sum d^2 - \left(\sum d\right)^2\right]$$ (3)

$$\sigma = \sqrt{\frac{\sigma^2 N}{N-1}}$$ (4)

$$\hat{d} = \frac{\sigma}{\sqrt{N-1}}.$$ (5)

Therefore, the computation of $\hat{d}$ involves three matrices: absorbed dose (d), number of interactions (N), and the sum of squares of absorbed dose (d^2).

2.4. Employed VRTs

2.4.1. Secondary particle production threshold
This technique is based on the definition of a stopping range value, which is the distance to be covered by the particle. When the particle has kinetic energy less than or equal to the equivalent of the defined stopping range, the production of secondary particles is stopped and the energy released from each interaction is deposited locally. The use of this technique is mandatory in Geant4, as it is applied to electrons in ionization and Bremsstrahlung processes to avoid divergence in the infrared range (Carrier *et al* 2004). The GATE command to set this distance is `SetCutInRegion`.

For comparison purposes, the threshold distances for producing secondary particles were set to 0.1, 2.0, 10.0, and 50.0 mm in the voxelized virtual phantom, while the `world` volume had the threshold fixed at 10.0 mm.

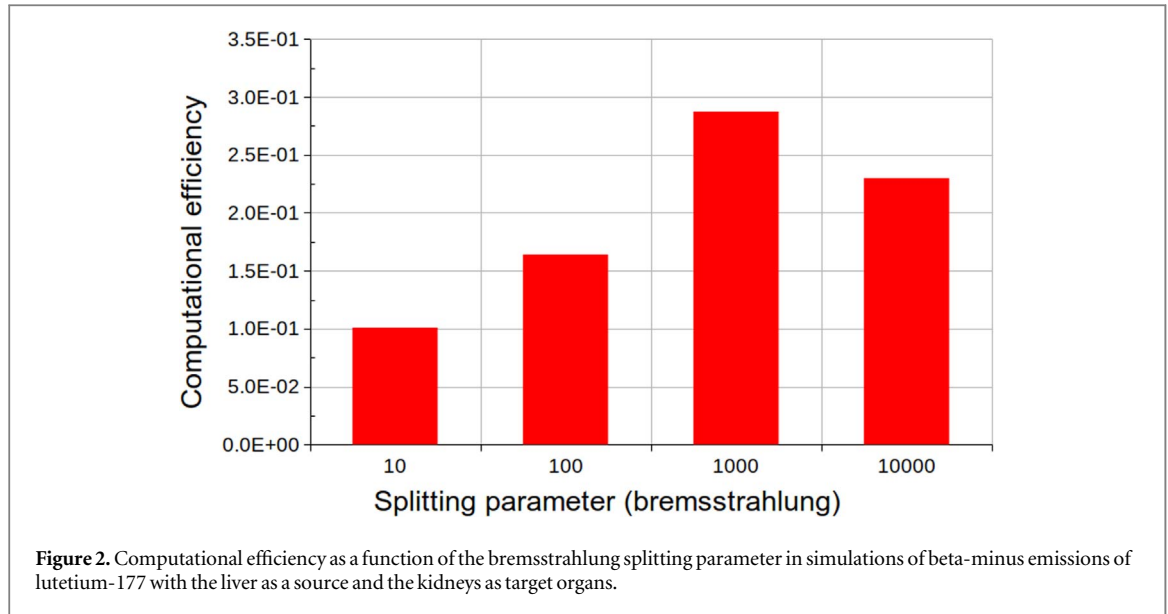#### 2.4.2. Particle kinetic energy cutoff
Geant4 electromagnetic models describe the interactions of particles with matter down to a finite energy value and the kinetic energy is deposited locally below this limit (Geant4-Collaboration 2022). The kinetic energy cutoff technique kills the track when it reaches a minimum remaining kinetic energy and deposits its energy locally, which is useful to accelerate the calculation of the absorbed dose of low-range heavy particles (Geant4-Collaboration 2021). The command used to set this energy value is `SetMinKineticEnergyInRegion`.

In this work, kinetic energy cut-off values were defined for charged particles, to ensure local deposition of their energy and reduce the computation time. The selected cut-off values were greater than the maximum energy of the particles emitted by the radionuclide because the absorbed dose was computed for the whole organ. However, if the absorbed dose should be determined on a smaller scale, such as a single voxel, the cut-off value should be chosen by considering the voxel size and the particle range. Hence, lutetium-177 had a kinetic energy cutoff for electrons set to 5 MeV and the alpha cutoff for radio-223 was defined as 12 MeV. This means each charged particle emitted from these radionuclides will have its energy deposited locally.

2.4.3. Bremsstrahlung and ionization splitting
This VRT is used to increase photon production from bremsstrahlung and ionization processes, within a known energy range, by a multiplier or splitting factor N. The weight of each secondary particle is $1/N$. This VRT can improve the precision of absorbed dose calculation without compromising the computing time (Geant4-Collaboration 2021). The GATE commands for Bremsstrahlung and ionization splitting are `/process/em/setSecBiasing eBrem` and `/process/em/setSecBiasing eIoni`, respectively.

The energy threshold value for the bremsstrahlung splitting must be defined to ensure that all photons are processed by this VRT. Thus, a 100 MeV threshold was chosen since it is higher than any energy of photon emissions enlisted in the ICRP 107. The splitting factor should be chosen to achieve the best computational efficiency and the feasibility of Monte Carlo dosimetry for clinical routine. For this task, four beta emission simulations with the liver as a source organ were performed, evaluating the computational efficiency of the absorbed dose calculation in the kidneys (target organs) by varying the splitting factor (figure 2). The splitting factor 1000 presented the highest computational efficiency, isotropically splitting the sampled bremsstrahlung

Figure 2. Computational efficiency as a function of the bremsstrahlung splitting parameter in simulations of beta-minus emissions of lutetium-177 with the liver as a source and the kidneys as target organs.

photon into 1000 parts if its energy is below 100 MeV. The same factor was also applied to the ionization process, which has a minor but non-negligible role in energy deposition.

2.4.4. TLE and seTLE

The track length estimator (TLE) method provides considerable variance reduction (Baldacci *et al* 2014). In this technique, a photon emitted as a primary particle deposits energy in all voxels it finds between the successive interaction points. The deposited energy represents the expected value that would be observed if a large number of identical primary photons were transported along the same path, instead of deposition of energy only in voxels contained in interaction points, as is the case in analogous Monte Carlo simulation. Secondary electrons are not tracked using the TLE and their energy is deposited locally, assuming that all energy released into the medium is absorbed by it. Therefore, this method considers the absorbed dose as approximately equal to the collision *kerma* (kinetic energy released in matter). TLE method can be used for primary photons with energy values up to 1 MeV interacting with tissues composed of elements with atomic numbers $Z \leqslant 20$ since the relative difference between linear energy-absorption and energy-transfer coefficients is below 1% (Attix 2004). At higher energies, an interaction of a photon with a tissue may create an electron with enough energy to deposit energy at a location away from the initial interaction position. For each step that occurs in the voxel *i* along the photon path, the absorbed dose is expressed as (Smekens *et al* 2014)

$$D_i^{\mathrm{TLE}} = \frac{E \times \mu_{en}(E, m_i) \times L_i}{\rho_i \times V}, \qquad (6)$$
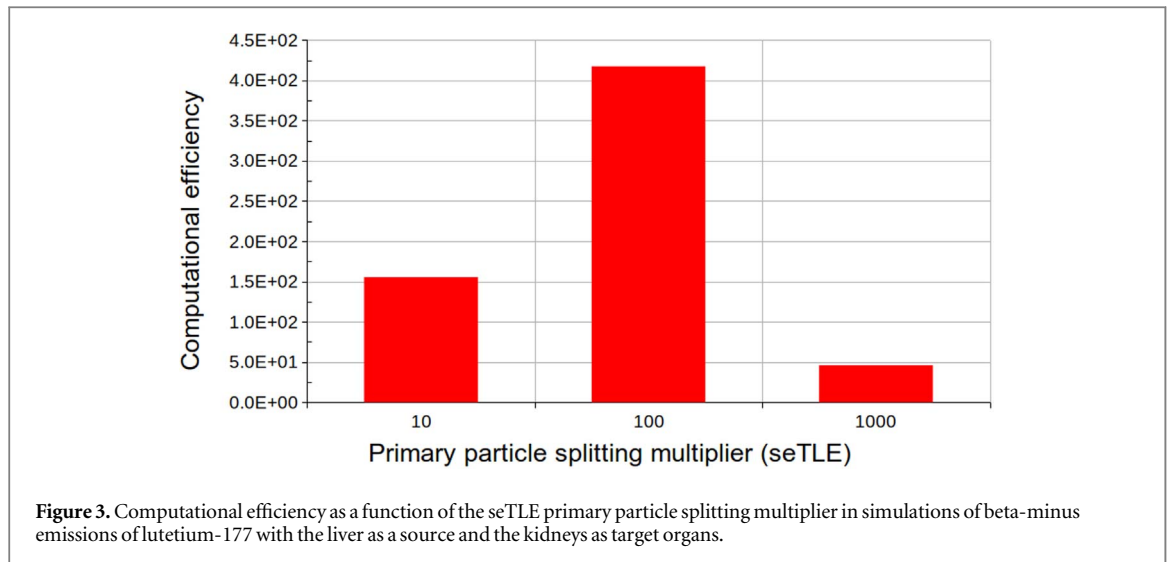
Where D_i^{TLE} is the dose deposited in voxel *i* of volume *V* and density ρ_i, $\mu_{en}(E, m_i)$ is the absorption coefficient for photon energy *E* in material m_i, and L_i is the step length of the photon in the voxel.

The split exponential track length estimator (seTLE) method combines three concepts to compute absorbed dose: Monte Carlo splitting, hybrid navigation, and expTLE (Smekens *et al* 2014). Each primary photon splits into *n* virtual particles at each interaction site, where *n* is the splitting multiplicity and the weight factor is 1/*n*. The primary photon is still tracked during simulation. The splitting procedure is applied for every new photon or change in energy/direction of an existing one. Each virtual particle is tracked using hybrid navigation, which is the replacement of these photons by hybrid particles, called hybridinos. Hybridinos do not have associated physical processes and therefore propagate the photons characteristics through any volume in a straight line. Only these virtual particles are used to calculate the dose distribution. Finally, the absorbed dose is determined using the expTLE method, which provides attenuation and energy absorption for each step. The photon weight is updated at each step using the Beer–Lambert law:

$$w_i^{\mathrm{out}} = w_i^{\mathrm{in}} \times \exp[-\mu(E, m_i) \times L_i], \qquad (7)$$

Where w_i^{out} and w_i^{in} are the output and input weights for each step of length L_i in material m_i, and $\exp[-\mu(E, m_i)$ is the attenuation coefficient of this material for photon energy *E*.

The absorbed dose in the current voxel D_i^{expTLE} is calculated from the integration of the infinitesimal energy deposited between positions *r* and *r* + d*r* as (Smekens *et al* 2009, 2014):

Figure 3. Computational efficiency as a function of the seTLE primary particle splitting multiplier in simulations of beta-minus emissions of lutetium-177 with the liver as a source and the kidneys as target organs.

$$dE = E\omega\mu_{en}dr \tag{8}$$

$$D_i^{\text{expTLE}} = \frac{\int_{r_{\text{in}}}^{r_{\text{out}}} dE}{\rho_i \times V} = \frac{E \times \mu_{en}(E, m_i) \times [w_i^{\text{in}} - w_i^{\text{out}}]}{\rho_i \times V \times \mu(E, m_i)}. \tag{9}$$

For simulations with the seTLE actor, it is necessary to define three commands: `enableHybridino`, `setPrimaryMultiplicity`, and `setSecondaryMultiplicity`.

Simulation time becomes longer as the seTLE splitting multiplier increases. Figure 3 shows the relationship between the splitting multiplier for primary particles and the computational efficiency for three simulations that estimate the absorbed dose in the gall bladder wall from a lutetium-177 gamma source uniformly distributed in the gall bladder contents. In this case, the splitting multiplier 100 provides the best computational efficiency.

2.4.5. Primary particle generator

A radioactive source can be simulated using its nuclear decay data, comprising the number of particles per nuclear transition. One of the methods used in this work is the `G4RadioactiveDecay` (Geant4-based radioactive decay processes) class (Agostinelli *et al* 2003), which simulates the radionuclide decay through the ion source type in GATE. Transitions, conversions, and emission probabilities are described using the evaluated nuclear structure data file (ENSDF) data (Bhat 1991). Another method to define the energy spectrum of the radioactive decay of a radionuclide is using the `energytype UserSpectrum` command and importing the nuclear decay data through the `setSpectrumFile` command. The particle energy may have a discrete value or obey a continuous distribution, represented by histograms. The yield values ($Yield_p$) can be used to fit the number of particles (N_p) that will be simulated in each decay (N_d) of the radionuclide used as a source, according to equation (10).

$$N_p = N_d \times Yield_p \tag{10}$$

The ICRP report 107 (Eckerman and Endo 2008) provides a nuclear decay database for dosimetric calculations of 1252 radionuclides. This database can be used in GATE through the `energytype UserSpectrum` command. Each emission type is adjusted with their respective yields to accurately simulate the radionuclide decay. The ICRP 107 publication provides the files ICRP-07.NDX, ICRP-07.RAD, ICRP-07.BET, ICRP-07.ACK and ICRP-07.NSF. The RAD file contains the discrete data on the energy and yield of each emitted radiation in nuclear transformations for each radionuclide. The BET file describes the beta spectrum for each beta emitter in the ICRP 107 collection. The spectral data is tabulated in a fixed logarithmic energy grid. For each radionuclide, the header record provides the name of the nuclide and the number of data records that contain the energy E (in MeV), and the number of electrons emitted by nuclear transformation with energy between E and $E + dE$. The NDX file serves as input to the RAD and BET files. It contains the radionuclide record fields that point to the radionuclide records in the RAD, BET, ACK, and NSF files. In addition to pointers, the record contains fields that inform the nuclide's physical half-life, decay mode, progeny identity (decay chain), the fraction of the nuclear transformations that generate each progeny (called branching fraction), the total energies emitted by alpha emissions, electrons and photons and other supporting data (Eckerman and Endo 2008). The ACK (Auger and Coster-Kronig electrons) and NSF (neutrons emitted per spontaneous fission)

Table 1. *S* values with the liver as source and target organ with and without the kinetic energy cutoff VRT applied for the beta emission of lutetium-177 and the alpha emission of radium-223.

Radionuclide	E_{min} (MeV)	$S\,[\mathrm{mGy} \times (\mathrm{MBq} \times \mathrm{s})^{-1}]$	ϵ
Lutetium-177	0 MeV (default)	$1.31 \times 10^{-5} \pm 1.04 \times 10^{-6}$	ϵ_1
	5 MeV	$1.32 \times 10^{-5} \pm 1.01 \times 10^{-6}$	$7.9\epsilon_1$
Radium-223	0 MeV (default)	$2.47 \times 10^{-3} \pm 1.66 \times 10^{-4}$	ϵ_1
	12 MeV	$2.47 \times 10^{-3} \pm 1.68 \times 10^{-4}$	$7.4\epsilon_1$

Table 2. *S* values for lutetium-177 beta-minus emission with the liver as a source organ for different secondary particle production threshold values.

Cutoff limit	VOI	$S\,[\mathrm{mGy} \times (\mathrm{MBq} \times \mathrm{s})^{-1}]$	ϵ
0.1 mm	*liver ← liver*	$1.31 \times 10^{-5} \pm 3.03 \times 10^{-7}$	ϵ_1
	kidneys ← liver	$1.38 \times 10^{-7} \pm 2.01 \times 10^{-8}$	ϵ_2
	GBW ← GBC**	$1.70 \times 10^{-5} \pm 3.49 \times 10^{-7}$	ϵ_3
2.0 mm	*liver ← liver*	$1.31 \times 10^{-5} \pm 3.03 \times 10^{-7}$	$1.10\epsilon_1$
	kidneys ← liver	$1.39 \times 10^{-7} \pm 2.03 \times 10^{-8}$	$1.10\epsilon_2$
	GBW ← GBC**	$1.70 \times 10^{-5} \pm 3.50 \times 10^{-7}$	$1.09\epsilon_3$
10.0 mm	*liver ← liver*	$1.31 \times 10^{-5} \pm 3.03 \times 10^{-7}$	$1.15\epsilon_1$
	kidneys ← liver	$1.39 \times 10^{-7} \pm 2.03 \times 10^{-8}$	$1.14\epsilon_2$
	GBW ← GBC**	$1.70 \times 10^{-5} \pm 3.49 \times 10^{-7}$	$1.13\epsilon_3$
50.0 mm	*liver ← liver*	$1.31 \times 10^{-5} \pm 3.03 \times 10^{-7}$	$1.14\epsilon_1$
	kidneys ← liver	$1.39 \times 10^{-7} \pm 2.03 \times 10^{-8}$	$1.13\epsilon_2$
	GBW ← GBC**	$1.70 \times 10^{-5} \pm 3.49 \times 10^{-7}$	$1.10\epsilon_3$

GBW (Gall Bladder Wall). **GBC** (Gall Bladder Content).

spectra files were not employed because they do not provide data for the selected radionuclides. However, Auger emission was simulated using data from the RAD file.

Following the pattern and arrangement of the records in the files mentioned above, a program was developed in the Python programming language to process data from the ICRP 107 files and generate a spectrum file for any radiation emitted by the radionuclides in the collection, standardized for reading in GATE simulations.

2.5. Computation efficiency

The computational efficiency (equation (11)) was calculated to compare the results for each scenario using VRTs:

$$\epsilon = \frac{1}{T\sigma^2}, \tag{11}$$

where *T* is the computational processing time to run a Monte Carlo simulation and σ is the relative uncertainty of the measurement in question, i.e. the absorbed dose.

The computational efficiency values in the comparisons are shown in a relative way, where the reference value is the computational efficiency of the simulations without the VRTs. The variables ϵ_1, ϵ_2, and ϵ_3 are used to differentiate the computational efficiencies between the simulations.

2.6. Reference data

The OpenDose collaboration (Chauvin *et al* 2020) provides a database of *S* values on its website, calculated from the average results of six different Monte Carlo codes (MCNP, EGS, Penelope, Fluka, Geant4, and GATE), using the voxelized anthropomorphic models made available by ICRP 110. These data will be compared with the results of this work to validate the sources defined using the methods described in 2.4.5.

3. Results

Tables 1–5, present the results with uncertainties. All simulations were performed with 10^7 primary particles, except by the results in table 2 where 10^8 particles were employed.

Table 1 shows the computation efficiency ϵ for the *S* values obtained with and without the kinetic energy cutoff VRT applied for the beta emission of lutetium-177 and the alpha emission of radium-223. The liver was the source and target organ and no bias was noticed in the results of both scenarios. The uncertainty of each *S*

Table 3. *S* values for lutetium-177 with the liver as source and target organs. Emission spectra were defined by ICRP 107 and G4RadioactiveDecay.

Source approach	$S\,[\text{mGy} \times (\text{MBq} \times \text{s})^{-1}]$	ϵ
`G4RadioactiveDecay`	$1.31 \times 10^{-5} \pm 1.04 \times 10^{-6}$	ϵ_1
ICRP 107 spectra	$1.31 \times 10^{-5} \pm 9.59 \times 10^{-7}$	$5.00\epsilon_1$

Table 4. *S* values for lutetium-177 beta-minus emission were determined using Bremsstrahlung/ionization splitting with gamma filter, i.e. only the absorbed dose from photons was computed.

Approach	target ← source	$S\,[\text{mGy} \times (\text{MBq} \times \text{s})^{-1}]$	ϵ
N/A	liver ← liver	$5.91 \times 10^{-9} \pm 1.21 \times 10^{-10}$	ϵ_1
	kidneys ← liver	$4.65 \times 10^{-10} \pm 1.23 \times 10^{-10}$	ϵ_2
	GBW* ← GBC*	$1.35 \times 10^{-5} \pm 1.15 \times 10^{-6}$	ϵ_3
e-Brem	liver ← liver	$5.89 \times 10^{-9} \pm 8.60 \times 10^{-11}$	$1.07\epsilon_1$
	kidneys ← liver	$4.32 \times 10^{-10} \pm 1.40 \times 10^{-11}$	$36.0\epsilon_2$
	GBW* ← GBC*	$1.34 \times 10^{-5} \pm 1.16 \times 10^{-6}$	$0.54\epsilon_3$
e-Ioni	liver ← liver	$5.86 \times 10^{-9} \pm 1.22 \times 10^{-10}$	$0.50\epsilon_1$
	kidneys ← liver	$4.02 \times 10^{-10} \pm 8.40 \times 10^{-11}$	$0.80\epsilon_2$
	GBW* ← GBC*	$1.34 \times 10^{-5} \pm 1.15 \times 10^{-6}$	$0.79\epsilon_3$
e-Brem and e-Ioni	liver ← liver	$5.89 \times 10^{-9} \pm 8.66 \times 10^{-11}$	$1.08\epsilon_1$
	kidneys ← liver	$4.39 \times 10^{-10} \pm 1.40 \times 10^{-11}$	$38.0\epsilon_2$
	GBW* ← GBC*	$1.34 \times 10^{-5} \pm 1.15 \times 10^{-6}$	$0.54\epsilon_3$

GBW (Gall Bladder Wall). **GBC** (Gall Bladder Content). **e-Brem** (electron Bremsstrahlung splitting). **e-Ioni** (electron Ionization splitting).

Table 5. *S* values for lutetium-177 gamma emission were determined using TLE and seTLE VRTs.

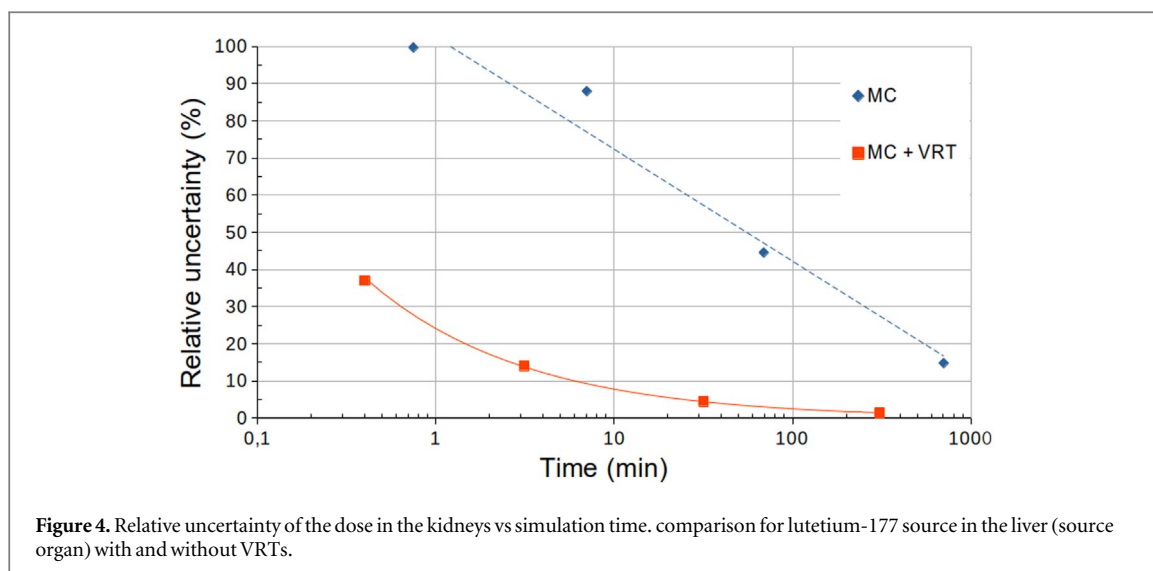| Approach	target ← source	$S\,[\text{mGy} \times (\text{MBq} \times \text{s})^{-1}]$	ϵ
N/A	liver ← liver	$4.77 \times 10^{-7} \pm 3.10 \times 10^{-7}$	ϵ_1
	kidneys ← liver	$1.17 \times 10^{-7} \pm 1.06 \times 10^{-7}$	ϵ_2
	GBW* ← GBC*	$2.58 \times 10^{-6} \pm 2.51 \times 10^{-7}$	ϵ_3
TLE	liver ← liver	$4.83 \times 10^{-7} \pm 5.12 \times 10^{-8}$	$4.50\epsilon_1$
	kidneys ← liver	$1.18 \times 10^{-7} \pm 2.83 \times 10^{-8}$	$2.80\epsilon_2$
	GBW* ← GBC*	$2.60 \times 10^{-6} \pm 3.82 \times 10^{-8}$	$29.40\epsilon_3$
seTLE	liver ← liver	$4.82 \times 10^{-7} \pm 4.22 \times 10^{-8}$	$5.10\epsilon_1$
	kidneys ← liver	$1.15 \times 10^{-7} \pm 1.84 \times 10^{-8}$	$3.90\epsilon_2$
	GBW* ← GBC*	$2.60 \times 10^{-6} \pm 1.51 \times 10^{-8}$	$62.50\epsilon_3$

GBW (Gall Bladder Wall). **GBC** (Gall Bladder Content).

value is about 7% of its respective value. The use of kinetic energy cutoff VRT provided a computational efficiency of 7.9 and 7.4 times larger for lutetium-177 and radium-223, respectively.

Table 2 describes the computation efficiency of a simulation with 10^8 primary particles of lutetium-177 beta emission by varying the secondary particle production threshold with values of 0.1, 2.0, 10.0, and 50.0 mm to compute the *S* value. No biased results were noticed for the selected threshold values. The secondary particle production threshold was set as 2.0 mm since the computation efficiency was practically constant for values larger than this. The uncertainty of each *S* value varied from 2% to 14% of its respective value.

Table 3 exhibits the *S* values for lutetium-177 with the liver as source and target organs, where the emission spectra were defined by the ICRP 107 through the GATE UserSpectrum and using the `G4RadioactiveDecay` class. The lutetium-177 source simulation based on ICRP 107 showed an overall computational efficiency of about 5 times when compared to the use of the `G4RadioactiveDecay` class. The uncertainty of each S value is about 7% of its respective value. No biased results were noticed for the selected radionuclide decay database.

Table 4 shows the splitting techniques applied to the Bremsstrahlung and ionization electromagnetic processes. No biases were noticed in the obtained *S* values for the selected VRTs. For the same number of

Figure 4. Relative uncertainty of the dose in the kidneys vs simulation time. comparison for lutetium-177 source in the liver (source organ) with and without VRTs.

Table 6. *S* values for lutetium-177, iodine-131, yttrium-90, and radium-223 in organs of interest were determined with the VRTs studied in this work and the OpenDose collaboration (Chauvin *et al* 2020).

Radionuclide	target ← source	S (this work) $\left[\frac{mGy}{MBq \times s}\right]$	S (OpenDose) $\left[\frac{mGy}{MBq \times s}\right]$	Percent error
Lutetium-177	liver ← liver	$1.32 \times 10^{-5} \pm 4.69 \times 10^{-10}$	$1.37 \times 10^{-5} \pm 9.13 \times 10^{-10}$	3.65%
	kidneys ← liver	$1.31 \times 10^{-7} \pm 1.57 \times 10^{-8}$	$1.35 \times 10^{-7} \pm 1.40 \times 10^{-8}$	2.96%
	$GBW^* \leftarrow GBC^*$	$1.72 \times 10^{-5} \pm 2.63 \times 10^{-9}$	$1.91 \times 10^{-5} \pm 1.68 \times 10^{-8}$	9.95%
	$SG^* \leftarrow SG^*$	$3.65 \times 10^{-4} \pm 4.40 \times 10^{-10}$	$3.77 \times 10^{-4} \pm 2.60 \times 10^{-8}$	3.18%
Iodine-131	lung ← thyroid	$3.06 \times 10^{-5} \pm 7.34 \times 10^{-11}$	$3.17 \times 10^{-5} \pm 3.32 \times 10^{-8}$	3.47%
	SW ← SC	$1.28 \times 10^{-5} \pm 2.18 \times 10^{-10}$	$1.31 \times 10^{-5} \pm 1.02 \times 10^{-8}$	2.29%
Yttrium-90	liver ← liver	$7.58 \times 10^{-5} \pm 2.10 \times 10^{-10}$	$7.93 \times 10^{-5} \pm 3.67 \times 10^{-9}$	4.41%
	kidneys ← liver	$1.62 \times 10^{-7} \pm 1.26 \times 10^{-8}$	$1.82 \times 10^{-7} \pm 1.37 \times 10^{-9}$	10.99%
	lung ← liver	$6.36 \times 10^{-7} \pm 2.63 \times 10^{-9}$	$6.29 \times 10^{-7} \pm 8.09 \times 10^{-10}$	1.11%
	IW ← IC	$2.45 \times 10^{-3} \pm 2.02 \times 10^{-10}$	$2.49 \times 10^{-3} \pm 6.30 \times 10^{-9}$	1.61%
Radium-223	liver ← liver	$1.42 \times 10^{-2} \pm 4.88 \times 10^{-10}$	$1.44 \times 10^{-2} \pm 4.60 \times 10^{-8}$	1.39%
	kidneys ← liver	$1.19 \times 10^{-2} \pm 4.48 \times 10^{-10}$	$1.20 \times 10^{-2} \pm 9.49 \times 10^{-8}$	0.83%

GBW (Gall Bladder Wall). **GBC** (Gall Bladder Content). **SG** (Salivary Gland). **SW** (Stomach Wall). **SC** (Stomach Content). **IW** (Intestine Wall). **IC** (Intestine Content).

primary particles, the relative uncertainty of the *S* values reached almost 25% without VRTs. The uncertainty of each *S* value varied from 2% to 8% of its respective value when using the splitting techniques.

The computational efficiency of the Bremsstrahlung splitting was 1.07 times higher with the liver as source and target volume (ϵ_1) and 36.0 times higher with the kidneys as the target volume. However, it was 0.54 times lower for the configuration *GBW ← GBC*. The solo use of ionization splitting showed no improvement in computational efficiency. Overall, the combination of both splitting techniques provided the best results, resulting in a computational efficiency 1.08 times higher with the liver as source and target volume (ϵ_1) and 38.0 times higher with the kidneys as the target volume, despite the 0.54 times lower for the configuration *GBW ← GBC*.

Specifically for photon emissions, the TLE and seTLE techniques showed enhanced computational efficiency, as seen in table 5. No biases were noticed in the obtained *S* values for the selected TLE and seTLE VRTs. For the same number of primary particles, the relative uncertainty of the *S* values reached almost 100% without VRTs and was kept under 10% when using them.

Using the TLE method and comparing it with a simulation without VRT, the computational efficiency was approximately 4.5 times higher with the liver as source and target volumes and reached 29.4 times higher in the configuration *GBW ← GBC*. Using the seTLE method, the computational efficiency was even better since the configuration *GBW ← GBC* provided a computation efficiency of 62.5 higher than without the use of the VRT.

To illustrate the capabilities of the employed VRTs in reducing processing time and, consequently, computational cost, another study was carried out: it consisted of two (*relative uncertainty of the dose in the kidneys* vs *simulation time*) graphs for eight simulations executed with lutetium-177 (figure 4) and another eight with radium-223 (figure 5). The liver was used as the source organ and the absorbed dose in the kidneys (organ

Figure 5. Relative uncertainty of the dose in the kidneys vs simulation time. comparison for radium-223 source in the liver (source organ) with and without VRTs.
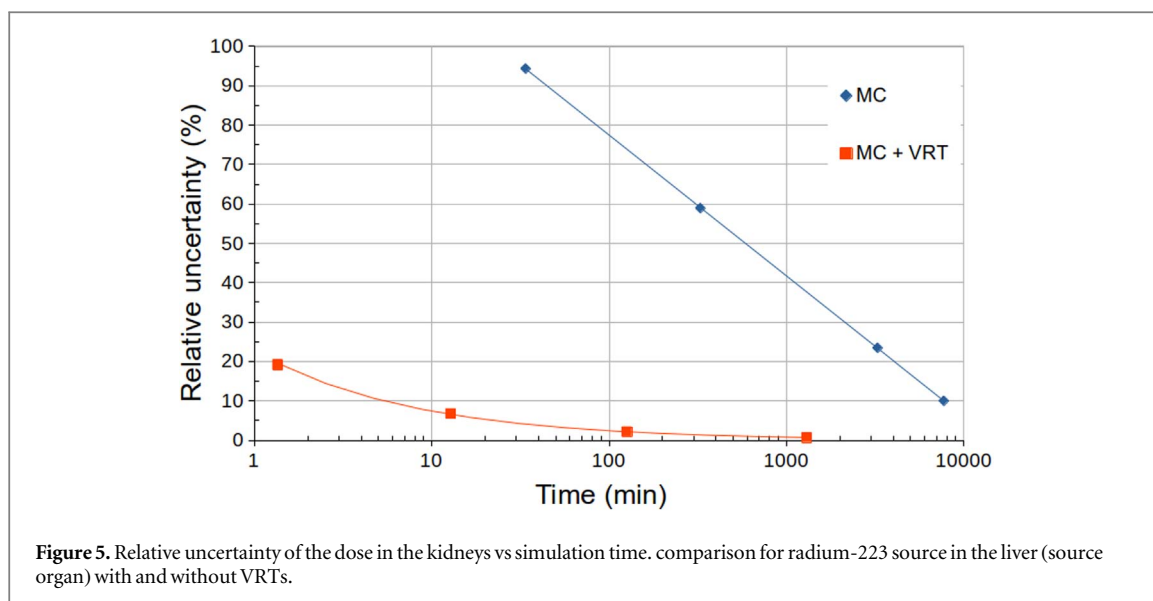
target) was calculated for four different numbers of events (10^5, 10^6, 10^7, and 10^8). Due to the natural distance between the liver and kidneys, only gamma-ray photons were considered. Bremsstrahlung photons also contribute to energy deposition, but to simplify this study, they were not taken into account. The sources of gamma emission from the decay of lutetium-177 and radium-223 were implemented through the energy emission spectra created from ICRP 107 data. Thus, eight simulations were performed without any variance reduction technique and another eight with the techniques secondary particle production limit and the seTLE actor, with this set being the best combination found for photon emissions. The threshold for producing secondary particles was set to 2.0 mm and the inputs for the seTLE actor were set with the commands *enableHybridino false, setPrimaryMultiplicity 100, and setSecondaryMultiplicity 1*. Using regression, the trend curve formulas were obtained and evaluated to calculate the simulation time with relative uncertainty at 10% (Karimipourfard *et al* 2022). Simulations with and without VRTs were performed at 6.1 min and 1176.0 min respectively for the lutetium-177 source, and 5.4 min and 7700.0 min respectively for the radium-223 source.

In table 6, the obtained *S* values were compared with the OpenDose database. Simulations were performed with secondary particle production threshold and source definition based on ICRP 107 energy spectra database. The adopted approach does not bias the results.

The maximum percent error perceived was 10.99 % and the lowest was 0.83%.

4. Discussion

Kinetic energy cutoff must be carefully chosen to estimate the absorbed dose in organs that receive cross-irradiation, as it could generate biased results when charged particles deposit all their energy locally when reaching the determined threshold value. For estimating absorbed dose from self-irradiating organs, where short-range charged particles are known to be protagonists in the energy deposition for a given radionuclide, setting a cutoff value for kinetic energy in simulations can drastically improve computational efficiency and at least maintain statistical quality. In fact, charged particles with high LET (e.g. alpha) are good candidates for the kinetic energy cutoff. On the other hand, using this VRT to estimate the absorbed dose by cross-irradiation can bias the result caused by the interruption of the secondary particle production when reaching the cut-off limit. Therefore, the energy fraction converted to bremsstrahlung should be determined to understand if its contribution is negligible or not to the absorbed dose in cross-irradiated organs.

The use of a spectrum-based source, such as those recorded in ICRP 107, can significantly increase computational efficiency and maintain similar statistics on the estimated absorbed dose in self-irradiating (or source) organs when compared to the `G4RadioactiveDecay` approach. In this case, other VRTs, such as the Bremsstrahlung/ionization splitting, can also be used to improve computational efficiency in regions that are affected by gamma emission but also receive a relevant contribution from radiation produced by Bremsstrahlung/ionization electromagnetic processes.

In dosimetric studies of sources with charged particle emissions (alpha and electrons), the techniques of kinetic energy cutoff, Bremsstrahlung, and ionization splitting showed a significant gain in computational

efficiency. Is not possible to apply Bremsstrahlung/Ionization splitting together with TLE and seTLE techniques since the last two methods do not produce secondary charged particles and transport only photons.

Furthermore, for photon emission, essentially gamma-rays and x-rays, TLE and seTLE showed a significant increase in computational efficiency, with seTLE being the best among them.

The secondary particle production threshold technique was effective in all emissions, being responsible for preventing the tracking of particles with energies that are negligible for the absorbed dose calculations performed in this study.

The definition of sources using the set of energy emission spectra obtained from ICRP 107 enabled the simulation of each type of specific radionuclide emission separately and thus allowed the application of VRTs properly for each situation, as well as could reduce the computation time by using computing parallelism in GATE. The `G4RadioactiveDecay` could also take advantage of computing parallelism at the run level since the Geant4-native multi-threading for event level parallelism is not currently supported in GATE.

The obtained percent errors are due to the fact that the OpenDose *S* values are the average of the results from simulations with six different Monte Carlo codes (Chauvin *et al* 2020).

The highlight of this work was the comparison of gamma-ray simulations from radionuclides lutetium-177 and radium-223 in the liver (source organ) to calculate the absorbed dose in the kidneys (target organ): the use of VRTs reduced the simulation time by a factor of 193 and 1426, respectively, when compared to simulations without VRTs, with a relative uncertainty of 10% (Karimipourfard *et al* 2022).

5. Conclusion

GATE VRTs were combined and implemented to compute the internal absorbed dose for radionuclides commonly used in Nuclear Medicine. The VRTs increased considerably the computational efficiency, maintaining or improving the statistical quality of the absorbed dose calculations in source and target volumes.

The improvements in the computational efficiency with the use of the VRTs were clearly verified when calculating the absorbed dose contribution from Bremsstrahlung photons, gamma emissions, and charged particles such as electron and alpha. However, it is important to have a good understanding of the processes that govern the interactions of radiation with matter to achieve the best computational efficiency without biasing the results. Therefore, the results of this work support the implementation of dosimetric calculations using Monte Carlo simulations in a feasible time, as low as a few minutes, to be employed in the clinical routine and web-based software.

Absorbed dose calculation can also be accelerated with computing parallelism, through the use of GPU, clusters, or FPGA.

Data availability statement

All data that support the findings of this study are included within the article (and any supplementary information files). Data will be available from 1 March 2023.

Conflict of interest statement

The authors have no relevant conflicts of interest to disclose.

ORCID iDs

Leanderson P Cordeiro ⬥ https://orcid.org/0000-0002-1150-1244
Rafael A Kitamikado ⬥ https://orcid.org/0000-0003-4205-3824
Daniel A B Bonifacio ⬥ https://orcid.org/0000-0002-0588-5720

References

Abhyankar Y *et al* 2019 *Phys. Med.* **64** 166–73

Agostinelli S *et al* 2003 *Nucl. Instrum. Methods Phys. Res.* A **506** 250–303

Attix F H 2004 *Introduction to Radiological Physics and Radiation Dosimetry* (Madison, Wisconsin: Wiley-VCH)

Baldacci F *et al* 2014 A track length estimator method for dose calculations in low-energy X-ray irradiations: implementation, properties and performance *Z. für Med. Phys.* **25** 36–47

Bhat M 1991 Evaluated nuclear structure data file (ensdf)

Bolch W, Eckerman K, Sgouros G and Thomas S 2009 *J. Nucl. Med: Official Publ., Soc. Nucl. Med.* **50** 477–84

Bonifacio D, Belcari N, Moehrs S, Moralles M, Rosso V, Vecchio S and Del Guerra A 2010 *Nucl. Sci., IEEE Trans.* **57** 2483–89

Bonifacio D A B, Sa L V, Costa G C A, Cordeiro L P and Amaral M G 2021 *Internal Radiation Dose* (http://www.irdose.com.br/)

Carrier J F, Archambault L, Beaulieu L and Roy R 2004 *Med. Phys.* **31** 484–92

Chauvin M *et al* 2020 *J. Nucl. Med.* **61** 10

Costa G, Bonifacio D, Sarrut D, Cajgfinger T and Bardiès M 2017 *Phys. Med.* **42** 292–7

Eckerman K and Endo A 2008 *Ann. ICRP* **38** 7–96

EL Bakkali J, Doudouh A and Mansouri H 2017 *Phys. Med.* **5**

Fedorov A *et al* 2012 *Magn. Reson. Imaging* **30** 1323–41

Frezza A, Joachim-Paquet C, Chauvin M and Després P 2020 *Phys. Med.* **73** 95–104

Geant4-Collaboration 2021 Geant4 a simulation toolkit—physics reference manual 2022 [Online; accessed 7. Mar. 2022] (https://geant4-userdoc.web.cern.ch/UsersGuides/PhysicsReferenceManual/fo/PhysicsReferenceManual.pdf)

Geant4-Collaboration 2022 Book for application developers (https://geant4-userdoc.web.cern.ch/UsersGuides/ForApplicationDeveloper/fo/BookForApplicationDevelopers.pdf) (Accessed on 02/10/2023)

Grosswendt B 2012 *Radiat. Prot. Dosim.* **150** 124–6

Guide for physics lists 2022 PhysicsListGuide.pdf (Accessed on 09/12/2022)

Jan S *et al* 2004 *Phys. Med. Biol.* **49** 4543–61

Jan S *et al* 2011 *Phys. Med. Biol.* **56** 881

Karimipourfard M, Sina S and Alavi M 2022 *Radiat. Phys. Chem.* **195** 110046

Lamrabet A, Maghnouj A, Tajmouati J and Bencheikh M 2021 *Nucl. Eng. Technol.* **53** 3164–70

Pareja G S *et al* 2021 Variance-reduction methods for Monte Carlo simulation of radiation transport *Front. Phys.* **9** 4

Peng Z, Fang X, Yan P, Shan H, Liu T, Pei X, Wang G, Liu B, Kalra M and Xu G 2020 *Med. Phys.* **47** 2526–36

Pinto G M, Bonifacio D A B, de Sá L V, Lima L F C, Vieira I F and Lopes R T 2020 *Phys. Med. Biol.* **65** 045010

Sarrut D *et al* 2014 *Med. Phys.* **41** 064301

Sarrut D *et al* 2021 *Phys. Med. Biol.* **66** 10

Sgouros G, Bodei L, McDevitt M and Nedrow J 2020 *Nat. Rev. Drug Discovery* **19** 589–608

Smekens F, Freud N, Létang J, Adam J F, Ferrero C, Elleaume H, Bravin A, Estève F and Babot D 2009 *Phys. Med. Biol.* **54** 4671–85

Smekens F, Létang J, Noblet C, Chiavassa S, Delpon G, Freud N, Rit S and Sarrut D 2014 *Phys. Med. Biol.* **59** 7703–15

Visvikis D, Bardiès M, Chiavassa S, Danford C, Kirov A, Lamare F, Maigne L, Staelens S and Taschereau R 2006 *Nucl. Instrum. Methods Phys. Res.* A **569** 335–40